Visualizing Rev1 catalyze protein-template DNA synthesis

Tyler M. Weaver[a,b,1] (ID), Luis M. Cortez[a,b,1] (ID), Thu H. Khoang[a,b], M. Todd Washington[c], Pratul K. Agarwal[d] (ID), and Bret D. Freudenthal[a,b,2]

[a]Department of Biochemistry and Molecular Biology, University of Kansas Medical Center, Kansas City, KS 66160; [b]Department of Cancer Biology, University of Kansas Medical Center, Kansas City, KS 66160; [c]Department of Biochemistry, University of Iowa, Iowa City, IA 52242; and [d]Department of Physiological Sciences and High-Performance Computing Center, Oklahoma State University, Stillwater, OK 74048

During DNA replication, replicative DNA polymerases may encounter DNA lesions, which can stall replication forks. One way to prevent replication fork stalling is through the recruitment of specialized translesion synthesis (TLS) polymerases that have evolved to incorporate nucleotides opposite DNA lesions. Rev1 is a specialized TLS polymerase that bypasses abasic sites, as well as minor-groove and exocyclic guanine adducts. Lesion bypass is accomplished using a unique protein-template mechanism in which the templating base is evicted from the DNA helix and the incoming dCTP hydrogen bonds with an arginine side chain of Rev1. To understand the protein-template mechanism at an atomic level, we employed a combination of time-lapse X-ray crystallography, molecular dynamics simulations, and DNA enzymology on the *Saccharomyces cerevisiae* Rev1 protein. We find that Rev1 evicts the templating base from the DNA helix prior to binding the incoming nucleotide. Binding the incoming nucleotide changes the conformation of the DNA substrate to orient it for nucleotidyl transfer, although this is not coupled to large structural changes in Rev1 like those observed with other DNA polymerases. Moreover, we found that following nucleotide incorporation, Rev1 converts the pyrophosphate product to two monophosphates, which drives the reaction in the forward direction and prevents pyrophosphorolysis. Following nucleotide incorporation, the hydrogen bonds between the incorporated nucleotide and the arginine side chain are broken, but the templating base remains extrahelical. These postcatalytic changes prevent potentially mutagenic processive synthesis by Rev1 and facilitate dissociation of the DNA product from the enzyme.

DNA polymerase | DNA repair | translesion synthesis

Cells are tasked with efficiently and faithfully replicating the genome in each round of cell division (1–3). During replication, the replicative DNA polymerases encounter a variety of DNA lesions that can stall the replication fork, promoting genomic instability (4, 5). One way the cell prevents this is through the recruitment of specialized translesion synthesis (TLS) polymerases that have evolved unique mechanistic and structural properties, rendering them capable of bypassing DNA lesions that stall the replication fork (6, 7). Although both replicative and TLS polymerases perform the same general nucleotidyl transferase reaction, in which they extend a newly synthesized daughter strand of DNA, the mechanistic details of the reactions differ among the two polymerase types in order to provide the proper efficiency and fidelity necessary for each. In the case of a replicative DNA polymerase, the enzyme binds an incoming deoxynucleotide triphosphate (dNTP) and two associated metal ions, while sampling for proper Watson–Crick base pairing to the templating base, ensuring faithful replication. In most cases, dNTP binding is coupled to a polymerase conformational change in which the enzyme closes around the nascent base pair. Moreover, upon proper organization of the active site, the primer terminal 3′-OH undergoes deprotonation and in-line nucleophilic attack at Pα of the incoming dNTP, resulting in the generation of a phosphodiester bond and a pyrophosphate (PP$_i$) moiety (1–3, 8–10).

Rev1 is an example of a specialized TLS polymerase and is also an important factor in the assembly of the TLS machinery. Rev1 is recruited to a stalled replication fork through interactions with monoubiquitinated proliferating cell nuclear antigen (PCNA) (11). Once at the stalled replication fork, Rev1 can act as a scaffolding protein by interacting with other TLS polymerases, which is important for polymerase switching during lesion bypass and extension (12–14). In addition to the critical role in organizing the TLS machinery, the DNA synthesis activity of Rev1 is utilized to preferentially bypass abasic sites as well as minor-groove and exocyclic guanine adducts (15–19). Importantly, Rev1 predominantly inserts cytosine over all other dNTPs, which is advantageous during bypass of bulky adducted guanine residues (20, 21). The first crystal structures of the Rev1 precatalytic ternary complex (Rev1/DNA/dCTP) revealed it uses a novel protein-templating mechanism for incoming nucleotide discrimination (22). In this mechanism, Rev1 displaces the templating guanine into an extrahelical position. The templating guanine is subsequently replaced by an arginine side chain, which acts as a protein-template to hydrogen bond with the Watson–Crick face of the incoming dCTP (23). Additional structures of Rev1 in complex with a templating abasic site, γ-HOPdG, and BP-N2-dG have shown Rev1 uses a similar mechanism to bypass multiple types of DNA damage (15, 24, 25).

Significance

Translesion synthesis (TLS) DNA polymerases bypass DNA damage that is unable to be accommodated by replicative DNA polymerase active sites. The TLS polymerase Rev1 bypasses a variety of DNA damage, including exocyclic guanine adducts and abasic sites using a unique protein-template mechanism. Using time-lapse X-ray crystallography, computational analysis, and enzyme kinetics, we provide insight into the protein-template mechanism used by Rev1. Our structural snapshots identify that movement of the primer DNA strand facilitates precatalytic organization of the Rev1 active site and phosphodiester bond formation. Additionally, we determine postcatalytic events, including pyrophosphate hydrolysis in the active site and an inability to reincorporate the templating guanine into the DNA helix, which ultimately prevents mutagenic processivity by Rev1.

Several unanswered questions regarding the Rev1 reaction mechanism hamper our understanding of how it catalyzes this unusual means of DNA synthesis. Namely, the protein template Rev1 uses for DNA synthesis requires the templating base be evicted from the active site and the surrogate Rev1 R324 protein-template positioned for binding the incoming dCTP. However, the order of events necessary for this precatalytic organization of the Rev1 active site remains elusive. Additionally, postcatalytic steps remain unknown at the atomic level. This includes how the dCMP disengages from the templating arginine and whether the templating base remains extrahelical after dCMP insertion. Finally, a molecular-level mechanism that limits Rev1 from performing multiple mutagenic cytosine insertions during TLS has not been deciphered. To address these outstanding questions, we have used a combination of time-lapse X-ray crystallography, molecular dynamic (MD) simulations, and biochemical approaches.

Results

To observe the Rev1 catalytic cycle at the atomic level, we employed time-lapse X-ray crystallography (Fig. 1A) (26–31). To accomplish this, we first generate binary Rev1/DNA complex crystals with a templating guanine. Importantly, Rev1 interacts with a templating guanine and damaged guanines in an identical manner (15, 24, 25). These binary Rev1/DNA crystals are subsequently transferred into a cryoprotectant solution containing dCTP and CaCl$_2$ to generate Rev1 ground-state ternary (Rev1/DNA/dCTP) complexes. Importantly, Ca^{2+} facilitates nucleotide binding but does not initiate catalysis (26–31). To initiate catalysis, the Rev1 ground-state ternary complex crystals are subsequently transferred to a cryoprotectant solution containing either MgCl$_2$ or MnCl$_2$. The crystals are then flash-frozen at various time points prior to collecting X-ray diffraction data (Fig. 1A). The resulting structures provide high-resolution snapshots of the Rev1/DNA complex during active site organization, catalysis, and postcatalytic events.

Precatalytic Organization of the Rev1 Active Site. To decipher the steps necessary for organization of the Rev1 active site, a 2.05 Å structure of the Rev1 binary complex was solved in space group P2$_1$2$_1$2$_1$ (*SI Appendix*, Table S1). In the Rev1 binary complex, the templating guanine (G$_t$) is evicted from the active site and displaced ~90° from the DNA helix (Fig. 1B). The evicted G$_t$ is stabilized within a hydrophobic pocket and forms hydrogen bonds between N7 and O6 of its Hoogsteen edge and the backbone amides of M685 and G686 in the Rev1 G-loop (Fig. 1B). The void generated by the evicted G$_t$ is occupied by residues R324 and L325 of the Rev1 N-digit helix (Fig. 1B). L325 has been hypothesized to be important for evicting and keeping the templating G$_t$ out of the DNA duplex, while R324 serves as the protein-template for binding the incoming dCTP through the Nε and Nη of the guanidinium group (Fig. 1B) (22). Displacement of the G$_t$ and the positioning of R324 as the protein-template is the first step in organizing the Rev1 active site for binding of the incoming dNTP.

To capture the ground-state ternary complex of Rev1 with an incoming dCTP, binary complex crystals were soaked in a cryoprotectant containing 5 mM dCTP and 50 mM CaCl$_2$ (Fig. 1A). The resulting crystal diffracted to 1.40 Å and is in the P2$_1$2$_1$2$_1$ space group (*SI Appendix*, Table S1). In the ternary complex, the G$_t$ remains in an identical conformation as observed for the binary complex (Fig. 1C). The incoming dCTP forms a planar hydrogen bonding interaction with the Nε and Nη of the R324 side chain via the O2 and N3 of the dCTP Watson–Crick edge (Fig. 1C). Structural superimposition of the binary and ternary complexes reveal the Rev1 active site does not undergo large conformational changes upon dCTP binding (Fig. 1D). Only subtle ~1.0 Å changes at residues D362 and D467 are observed upon nucleotide binding and metal coordination. In contrast, substantial structural changes occur upon dCTP binding at the primer terminus. The 5′ phosphate backbone of the primer terminal dG is shifted 2.5 Å compared to the position in the binary state (Fig. 1E). The R518 side chain, which coordinates the nonbridging oxygen of the 5′ dG phosphate backbone, shifts 4.4 Å to track the primer strand movement (Fig. 1E). This shift in the primer strand results in a 1.8 Å shift of the primer terminal 3′-OH toward the Pα of the incoming dCTP (Fig. 1D). These movements result in the 3′-OH of the primer terminus being 3.7 Å from Pα of the incoming dCTP and in proper orientation for in-line nucleophilic attack. Together, the Rev1 binary and ternary complex structures indicate that movement at the primer terminus is important for precatalytic organization of the Rev1 active site.

Characterizing Rev1 Catalyze Protein-Template DNA Synthesis. To capture structural snapshots during catalysis, Rev1/DNA/dCTP ternary complex crystals were transferred to a second cryoprotectant lacking dCTP and containing MgCl$_2$ instead of CaCl$_2$ for 5 min (Fig. 1A). The resulting crystal diffracted to 1.80 Å and was in space group P2$_1$2$_1$2$_1$ (*SI Appendix*, Table S1). This intermediate structural snapshot contained both reactant (dCTP) and product (dCMP and PP$_i$) states, as evident by electron density between Pα and Pβ as well as the 3′-OH and Pα, respectively (Fig. 2A). Occupancy refinement determined the reaction is ~30% product and ~70% reactant. The position of active site residues and metal ions remain identical to the ground-state ternary complex, thus indicating the Rev1 protein does not undergo large structural changes during catalysis. In contrast, significant movement occurs in the primer DNA strand that coincides with phosphodiester bond formation. The 5′ phosphate backbone of dG, formerly the primer terminal nucleotide, is in two conformations. The product conformation is shifted 4.0 Å proximal from the conformation in the reactant conformation (Fig. 2B). This coincides with a 5.4 Å shift of R518, which coordinates the 5′ backbone phosphate of the dG (Fig. 2B). The inserted dCMP in the product state shifts toward the primer terminal base pair by 1.1 Å compared to the incoming dCTP in the ground state, resulting in a loss of planarity between the dCMP and R324 (Fig. 2B). The change in conformation of the inserted dCMP after bond formation likely disrupts the hydrogen bonding interaction between R324 and the Watson–Crick face of the inserted dCMP.

To obtain a product complex, ternary complex crystals (Rev1/DNA/dCTP) were soaked in a cryoprotectant containing MgCl$_2$ for 10 min (Fig. 1A). The resulting crystal diffracted to 2.20 Å and shows the nucleotidyl transfer reaction is complete (Fig. 2C and *SI Appendix*, Table S1). Consistent with the prior structural snapshots, the structural changes observed postcatalysis are isolated to the primer DNA strand and not the Rev1 protein. The inserted dCMP shifts 1.7 Å toward what was the primer terminal dG, which results in a loss of planarity between the dCMP and R324 (Fig. 2D). The distances between R324 and the Watson–Crick edge of the inserted dCMP are now 2.9 Å and 3.0 Å. This combined with the loss in planarity indicates the hydrogen bonding interaction between dCMP and R324 is lost or weakened (Fig. 2D). In addition, the dCMP is more dynamic in the product complex with a B-factor of 43.07 Å^2 compared to 12.40 Å^2 for the incoming dCTP in the ground-state ternary complex. The primer DNA strand also undergoes additional movement during product formation. The 5′ backbone phosphate of the dG, formerly the primer terminal nucleotide, exists in two conformations. Conformation one is similar to the conformation in the ground-state ternary complex. In the second conformation, the dGMP 5′ backbone phosphate has moved 4.2 Å proximal to the position in the ternary complex (Fig. 2D). Similar to the transition from binary to ternary complex, the two conformations of R518 track the two conformations of the dGMP 5′ backbone phosphate.

To understand the role of R518 in Rev1 catalysis, a R518A Rev1 mutant was generated. Kinetic parameters were obtained for the insertion of dCTP by both the R518A variant and WT Rev1 protein. The steady-state kinetic analysis revealed Rev1 R518A has a k_{cat} of $0.022 \pm 1.3 \times 10^{-4}$ min, which is almost identical to Rev1 WT at $0.019 \pm 7.8 \times 10^{-5}$ min (Fig. 2 E and F). In contrast, Rev1 R518A has an ~15-fold lower K_m (dCTP) (28.32 ± 4.49 µM) than Rev1 WT (2.16 ± 0.25 µM), indicating that R518 is important for incoming dCTP binding (Fig. 2 E and F). To understand the potential role of R518A in nucleotide binding, a ground-state ternary structure of Rev1 R518A with an incoming dCTP was solved to 1.64 Å (*SI Appendix*, Table S1). The overall structure of WT and R518A Rev1 in the ternary ground-state structures is very similar with an RMSD (Cα) of 0.109. In addition, the Rev1 active site, including the conformation of R324, L325, the incoming dCTP, and metal coordinating residues is identical between the two structures (*SI Appendix*, Fig. S1). However, B-factor analysis revealed that the 3′-OH of the primer terminus in the R518A ternary ground-state structure was more dynamic at 17.26 Å^2 when compared to the 3′-OH in the WT ternary ground-state structure at 13.92 Å^2. This is likely due to disruption of the hydrogen bonding between R518 and the nonbridging oxygen of the 5′ dG phosphate backbone in the R518A mutant Rev1 protein (*SI Appendix*, Fig. S1*B*). Together, these data are consistent with R518 playing an important role in stabilizing movement of the primer terminus to organize the active site for incoming nucleotide binding.

MD Simulations of Rev1. To gain insight into the dynamics within the Rev1 active site during the catalytic cycle, we employed computational modeling of the Rev1 binary, ternary ground-state, and product structures. These MD simulations were performed for 1 µs and provide insight into the interactions of the evicted G_t, incoming dCTP, and inserted dCMP. The X-ray crystal structures show the evicted G_t is stabilized via hydrogen bonds between N7 and O6 of the Hoogsteen edge with the backbone amides of M685 and G686, respectively (Figs. 1 and 2). By monitoring these hydrogen bonding distances throughout the simulation, we gained insight into the stability of the extrahelical G_t. During the binary simulation, these interactions were broken around 220 ns of the MD simulation, as indicated by the increased distance between M685$_n$–N7 and G686$_n$–O6 (Fig. 3*A*, black line). This results in the G_t returning back to the intrahelical orientation within the DNA helix. In contrast, the G_t remained extrahelical for the entire MD simulation of the ternary (dCTP bound) and product (dCMP inserted) complexes, as indicated by the constant hydrogen bonding distances between M685$_n$–N7 and G686$_n$–O6 (Fig. 3*A*, red and green lines). Together these simulations indicate the templating G_t remains extrahelical upon binding and insertion of the incoming dCTP.

To characterize the dynamics of the incoming dCTP and inserted dCMP, we monitored the distances between the Nε and Nη2 of R324 and O2 and N3 of the dCTP, respectively, for the Rev1 ternary ground-state and product complex. The ternary ground-state MD simulation indicates R324 interacts strongly with the incoming dCTP; while in the product complex MD simulation, the inserted dCMP is dynamic and breaks the structural contacts with R324. In the ternary ground-state complex, short, and stabilizing hydrogen-bonding interactions (<3 Å) were observed to be present between R324 and the incoming dCTP for the entire 1-µs simulation (Fig. 3*B*, black line). In contrast, the interactions between the inserted dCMP and R324 were broken immediately at the start of the simulation of the product complex (Fig. 3*B*, red line). In the product complex, the inserted dCMP is very dynamic and adopts multiple orientations with conformations sampling both in and out of the DNA helix (Fig. 3*D*), while in the case of ternary ground-state complex the structural interactions appear to keep the dCTP bound in a single conformation and hydrogen bonding to R324

(Fig. 3*C*). This result is consistent with the inserted dCMP breaking the hydrogen-bonding interaction with R324 postcatalysis. Of note, throughout the product complex simulation the inserted dCMP does not hydrogen bond to the evicted G_t.

PP$_i$ Breakdown in the Rev1 Active Site. The canonical DNA polymerase reaction results in phosphodiester bond formation and the generation of PP$_i$. Interestingly, we did not observe PP$_i$ in the Rev1 product complex and instead observed density for two monophosphates (P$_i$) corresponding to Pβ and Pγ (Fig. 2*C*). This indicates hydrolysis of PP$_i$ occurred in the Rev1 active site after dCMP insertion, which is consistent with recent time-resolved crystallography with DNA Pol IV (32). The two P$_i$ in the Rev1 active site are no longer bound by a nucleotide associated metal, but remain stabilized in the active site by the positively charged side chains of R408 and K525 (Fig. 4*A* and *SI Appendix*, Fig. S2*B*). In addition, subtle structural changes occur to alleviate the electrostatic repulsion from the negatively charged species within the Rev1 active site. The Pβ has shifted 2.7 Å away from D362 and D467, while remaining stabilized by the positively charged side chain of R408. In contrast, the Pγ conformation is similar to the ground-state ternary complex; however, D362 has shifted by 1.7 Å and rotated 45° away from Pγ in the product structure. The lack of movement in the Pγ conformation is due to stabilization by side chains R408 and K525 (Fig. 4*A* and *SI Appendix*, Fig. S2*B*).

To determine the events that occur following PP$_i$ hydrolysis, two additional structures were determined after 15- and 30-min soaks in MgCl$_2$. After 15 min, the Rev1/DNA product structure diffracted to 2.05 Å and was in space group P2$_1$2$_1$2$_1$ (*SI Appendix*, Table S1). In this structure, the Pβ has disassociated from the active site and an ammonium ion from the crystallization solution is bound to the Pβ binding site (Fig. 4*B* and *SI Appendix*, Fig. S2*C*). In contrast, the Pγ remains stabilized in the active site by R408 and K525 and is in a similar conformation to the 10-min product structure (*SI Appendix*, Fig. S2). After a 30-min soak in MgCl$_2$, the Rev1/DNA product structure diffracted to 1.70 Å and was in space group P2$_1$2$_1$2$_1$ (*SI Appendix*, Table S1). In this structure, the Pγ has dissociated from the active site and is replaced by a water molecule, while a Cl$^-$ ion is now bound in the Pβ binding site (Fig. 4*B* and *SI Appendix*, Fig. S2*D*). These structural snapshots indicate that Rev1 utilizes a stepwise release of monophosphates with Pβ dissociating prior to Pγ, which is mediated by the differential stabilization of Pβ and Pγ by R408 and K525 (*SI Appendix*, Fig. S2). After monophosphate dissociation, the active site residues of Rev1 are in the same conformation as the binary (Rev1/DNA) structure, indicating that Rev1 has returned to the prenucleotide binding state.

To characterize the hydrolysis of PP$_i$ by Rev1 in solution, we performed a primer extension assay while monitoring the amount of PP$_i$ or monophosphate generated by Rev1. The primer extension reactions resulted in ~30-fold more monophosphate (10.89 ± 1.12 µM) than PP$_i$ (0.35 ± 0.15 µM), consistent with Rev1-mediated PPi hydrolysis during dCTP insertion (Fig. 4*D*). To determine if Rev1 can breakdown PP$_i$ without DNA, we monitored the conversion of PP$_i$ to monophosphate in the absence of primer-template DNA. The reaction with only Rev1 and PP$_i$ present resulted in the generation of 0.31 ± 0.08 µM monophosphate (Fig. 4*D*), which is similar to the background assay level of 0.48 ± 0.18 µM monophosphate determined without Rev1 present (Fig. 4*D*). This indicates that Rev1 must be bound to a primer-template DNA to perform PP$_i$ hydrolysis. Next, we tested if Rev1 mediated PP$_i$ hydrolysis is independent of dCTP insertion by monitoring the generation of monophosphate with only Rev1, PP$_i$, and primer-template DNA present. This reaction resulted in the generation of 3.52 ± 0.04 µM monophosphate (Fig. 4*D*). This indicates that the Rev1/DNA complex is able to perform PP$_i$ hydrolysis independent of the nucleotidyl transfer reaction.

Pyrophosphate hydrolysis in a polymerase active site is proposed to make the nucleotidyl transfer reaction energetically
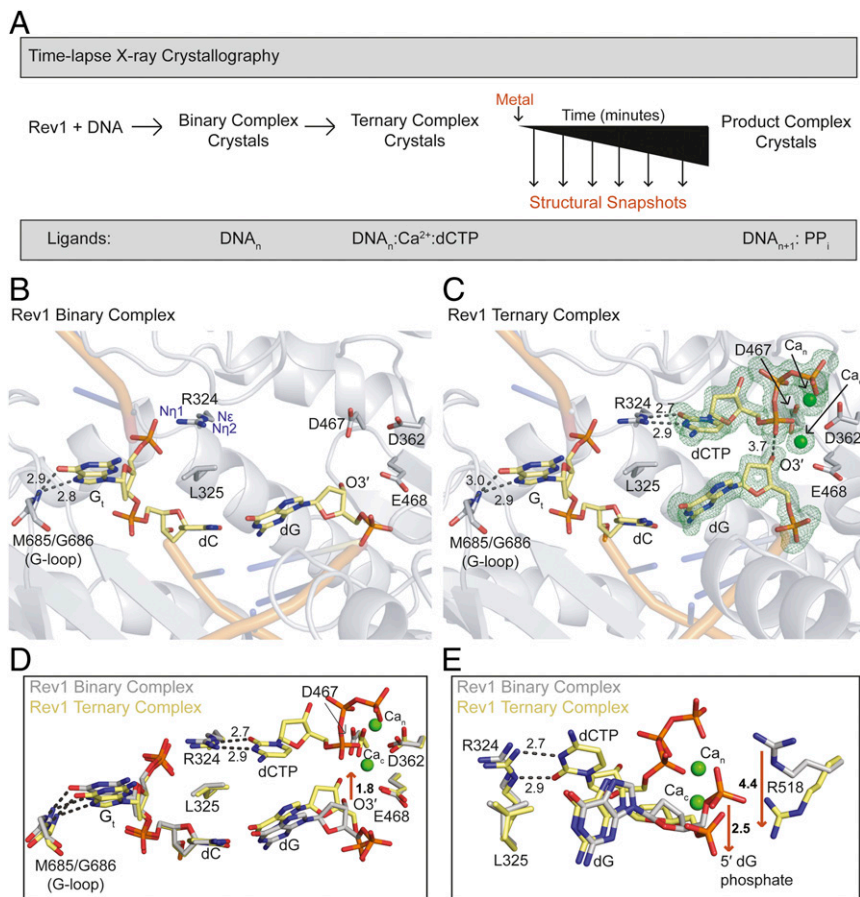
Fig. 1. Rev1 binary and ternary crystal structures. (*A*) The time-lapse X-ray crystallography approach. The ligands bound to each Rev1 state are indicated at the bottom. An active site close-up of the Rev1 (*B*) binary and (*C*) ternary crystal structures. The nucleic acid residues are shown in yellow and Rev1 in gray. A *Fo–Fc* OMIT map contoured at $\sigma = 3.0$ around the two active-site calcium ions, incoming dCTP, and primer terminal dG is shown as a green mesh. (*D* and *E*) An overlay of the Rev1 binary (gray sticks) and ternary (yellow sticks) complexes are shown in two orientations to indicate the movement at the primer termini, phosphate backbone, and R518. Key protein and DNA residues are indicated in each panel.

favorable (32). However, it also may be important for preventing the reverse reaction or pyrophosphorolysis, which results in the removal of the inserted nucleotide and generation of dNTP. To determine if Rev1 can perform the reverse reaction, pyrophosphorolysis experiments were performed on a primer-template DNA containing a templating guanine across from cytosine, which mimics the product state after Rev1-mediated insertion. After 60 min, we found minimal pyrophosphorolysis with Rev1 generating $14.4 \pm 1.0\%$ product (Fig. 4 *E* and *F*). For comparison, we performed pyrophosphorolysis experiments using a gapped DNA substrate and DNA polymerase β, a model polymerase used extensively to study the reverse reaction (27, 33–35). Under the same experimental conditions as those tested for Rev1, we found robust pyrophosphorolysis with DNA polymerase β generating $78.0 \pm 8.5\%$ product after only 5 min (*SI Appendix*, Fig. S3). These data indicate that Rev1 is inefficient at performing pyrophosphorolysis, which is likely due to Rev1 mediated PP$_i$ hydrolysis in the active site prior to performing the reverse reaction.

Rev1 Processivity. The three Rev1/DNA product structures indicate the G$_t$ remains extrahelical after catalysis has occurred. This suggests that Rev1 may be unable to shift register or translocate to the next base to continue DNA synthesis with additional cytosine insertions. To better understand Rev1 processivity in solution, a primer extension assay was designed. In this assay, Rev1 is preincubated with a fluorescein-labeled DNA substrate and

the reaction is then initiated with MgCl$_2$ and 150-fold excess of nonlabeled trap DNA. This reaction allows for Rev1 to continue primer extension until it dissociates from the DNA and is sequestered from its substrate by the trap DNA. In the presence of MgCl$_2$, Rev1 largely extends the primer-template DNA strand by only a single nucleotide before it dissociates, although a second, less efficient, insertion event is seen at higher dCTP concentrations, suggesting Rev1 may translocate to the next templating base (Fig. 5*A*). To determine if additional insertion of the second nucleotide could be achieved, the primer extension assay was performed using MnCl$_2$. Mn^{2+} is often used as an alternative metal cofactor when studying DNA polymerase mechanism, as it enhances both nucleotide binding and catalysis. Attempts to obtain robust insertion of the second nucleotide using physiological Mn^{2+} concentrations (0.05 mM) and a concentration commonly used for studying DNA polymerases (0.5 mM) were unsuccessful (*SI Appendix*, Fig. S4). In an attempt to get substantial insertion of the second nucleotide, we performed the processivity assay in the presence of 5 mM Mn^{2+}. In the presence of 5 mM Mn^{2+}, the processivity assay revealed robust insertion of one or two dCMPs before dissociation of Rev1 from the DNA substrate (Fig. 5*B*). Notably, 5 mM Mn^{2+} is in excess of the physiological concentrations found in the cell. However, the substantial second dCMP insertion by Rev1 in the presence of 5 mM Mn^{2+} allowed us to capture a structural snapshot of Rev1 inserting a second nucleotide using time-lapse X-ray crystallography.
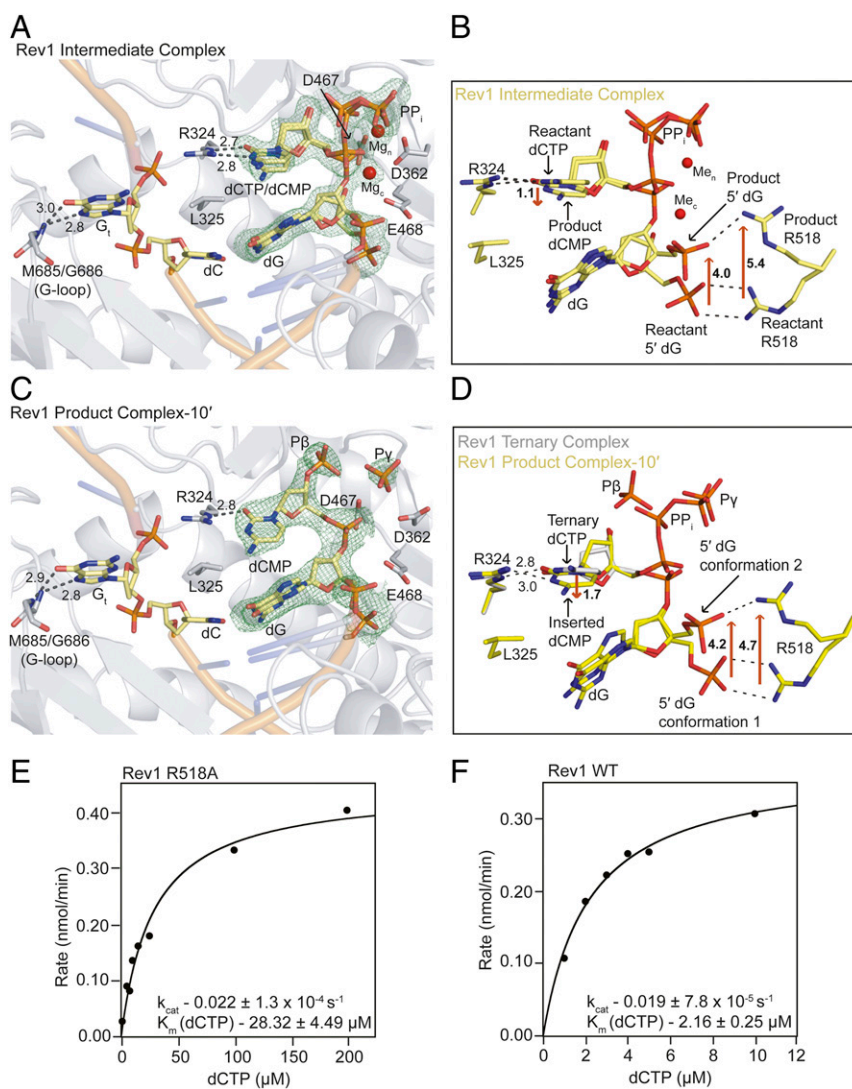
Fig. 2. Rev1 protein-templated DNA synthesis. (A) An active site close-up of the Rev1 intermediate crystal structure. The nucleic acid residues are shown in yellow and Rev1 in gray. An Fo–Fc OMIT map contoured at $\sigma = 3.0$ is shown as a green mesh. (B) A focused view of the structural movements in the Rev1 intermediate complex. The reactant and product states are indicated. The red arrows and distances (Å) highlight significant conformational differences. (C) An active site close-up of the Rev1 product complex after a 10-min soak in $MgCl_2$. An Fo–Fc OMIT map contoured at $\sigma = 3.0$ is shown as a green mesh. (D) A focused view of the active site of the product complex (yellow sticks) with an overlay of the dCTP from the Rev1 ternary complex (gray sticks) shown for reference. Red arrows and distances (Å) are indicated to highlight significant movements. Plots of the steady-state kinetics for (E) R518A and (F) WT Rev1 are shown with the k_{cat} and K_m (dCTP) indicated for each graph. Steady-state kinetics were performed in triplicate.

To capture a structural snapshot of Rev1 inserting a second nucleotide, Rev1/DNA ternary complex crystals were soaked in a cryoprotectant containing $MnCl_2$ for 240 min. The resulting crystal diffracted to 1.98 Å and was in space group $P2_12_12_1$ (*SI Appendix*, Table S1). In the Mn^{2+}-mediated product structure, Rev1 has inserted a dCMP and bound a second incoming dCTP. The inserted dCMP, now at the n-1 position, has been displaced into the major groove to accommodate a second bound dCTP within the active site (Fig. 5 C and D). Despite insertion of a dCMP, and the binding of a second dCTP, the evicted G_t remains extra helical and Rev1 has not translocated to the next templating base. L325 is thought to be important for eviction of the G_t from the DNA helix, as it occupies the void generated by the displaced G_t. To understand the contribution of L325 in preventing reincorporation of the G_t into the DNA duplex, a Rev1 L325G mutant was generated. We then crystallized the Rev1 L325G binary complex. These crystals were transferred to a cryoprotectant containing dCTP and $MnCl_2$ for 20 min. The resulting crystal diffracted to 2.55 Å and was in space group $P2_12_12_1$ (*SI Appendix*, Table S1). This structure showed that a single dCMP has been inserted and a second dCTP bound in the active site of Rev1, similar to the WT Rev1 $MnCl_2$ product complex (Fig. 5E). The void generated by the L325G mutation is now occupied by the inserted dCMP, but the G_t remains extra-helical (Fig. 5F). Together, these data indicate that reincorporation of the G_t and base pairing with the dCMP likely requires dissociation of Rev1 from the DNA substrate and poses a barrier to Rev1 processivity.

Discussion

Here, we utilized time lapse X-ray crystallography, MD simulations and enzyme kinetics to characterize protein-template DNA synthesis by Rev1. We identified movements of the DNA primer terminus that are important for both active site organization
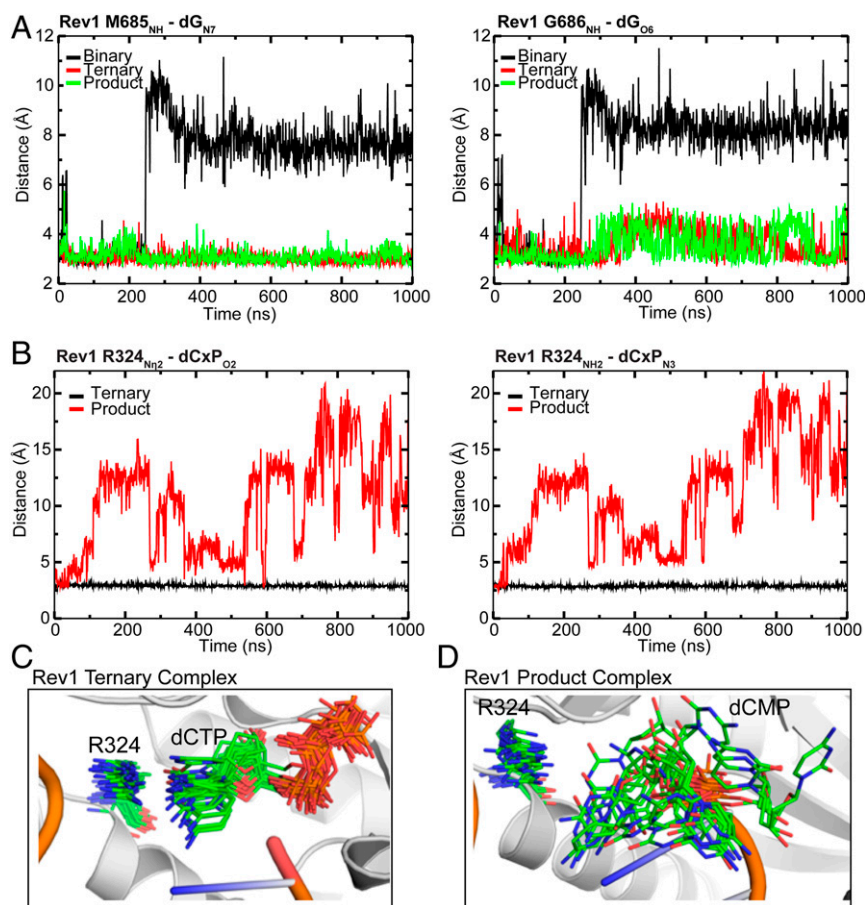
Fig. 3. MD simulations of Rev1 binary, ternary, and product complexes. (*A*) Distance profiles for the M685$_N$–N7 (*Left*) and the G686$_N$–O6 (*Right*) in the Rev1 binary (black line), ternary (red line), and product (green line) MD simulations. This behavior was reproduced by a second independent trajectory in which the interactions break after about 200 ns. (*B*) Distance profiles for the R324$_{NE}$ and dCTP$_{O2}$ (*Left*) and the R324$_{Nn2}$ and dCTP$_{n3}$ (*Right*) in the Rev1 ternary (black line) and product (red line) MD simulations. The average distance between these atoms is indicated for the entire trajectory. (*C*) Twenty conformations from MD simulations for the product complex (each 50-ns apart) showing the conformation of dCTP and R324. (*D*) Twenty conformations from MD simulations for the ternary complex (each 50-ns apart) showing the conformation of dCTP and R324.

before catalysis and disassociation of the products after catalysis. In addition, we found Rev1 hydrolyzes PP$_i$ after phosphodiester bond formation and releases the monophosphates from the active site in a stepwise manner. These structural snapshots also provide insight into the mechanism by which Rev1 prevents processive nucleotide incorporation to avoid aberrant insertions of cytosines after lesion bypass. Taking these data together, this work provides a fundamental advance in our understanding of how Rev1 catalyzes protein-template DNA synthesis.

Organization of Substrates and Products within the Rev1 Active Site. DNA polymerases bind the DNA and incoming nucleotide substrates and arrange them such that the 3′-oxygen of the primer termini and the α-phosphate of the incoming nucleotide are properly oriented for the nucleotidyl transfer reaction (1–3, 8–10). This occurs in two sequential steps: DNA binding and subsequent dNTP binding. In the case of most DNA polymerases, the DNA-binding step involves the DNA substrate binding to an open form of the polymerase. The duplex region of the DNA is approximately B-form, and the template base is positioned helically: That is, it is positioned such that it would form a normal helical Watson–Crick base pair if the correct nucleotide were to bind opposite it. Our structure of the Rev1/DNA binary complex shows that Rev1 differs from other DNA polymerases in the DNA binding step. DNA binding by Rev1 involves displacement of the G$_t$ from the DNA helix with R324 and L325

filling the space in the helix vacated by the flipped-out G$_t$. Importantly, the position of R324 in the binary complex is poised for dCTP binding and is analogous to the position of the templating DNA base in the structures of other polymerase/DNA binary complexes.

In the case of many DNA polymerases, the nucleotide-binding step couples the association of the nucleotide and metal ions to conformational changes in the polymerase (1–3, 8–10). Typically, this involves an open-to-closed transition of the finger subdomain around the incoming nucleotide and the template base. These large conformational changes facilitate the organization of the DNA and incoming nucleotide substrates for optimal catalysis. Our structure of the Rev1 ternary complex shows that Rev1 does not use such a concerted mechanism to organize substrates within its active site. No large changes in the structure of the protein are observed upon incoming nucleotide binding. Instead there is substantial movement of the primer DNA strand to reposition the primer terminal 3′-OH for an in-line nucleophilic attack on the α-phosphate of the incoming nucleotide. Despite the unique mechanism Rev1 uses for nucleotide binding, the resulting active site orientation for in-line nucleophilic attack on the α-phosphate is identical to other DNA polymerases.

In the product complex of other DNA polymerases, the incorporated nucleotide is base-paired with the templating base (1–3, 8–10). The base-paired product is then released from the active site through reopening of the finger subdomain of the
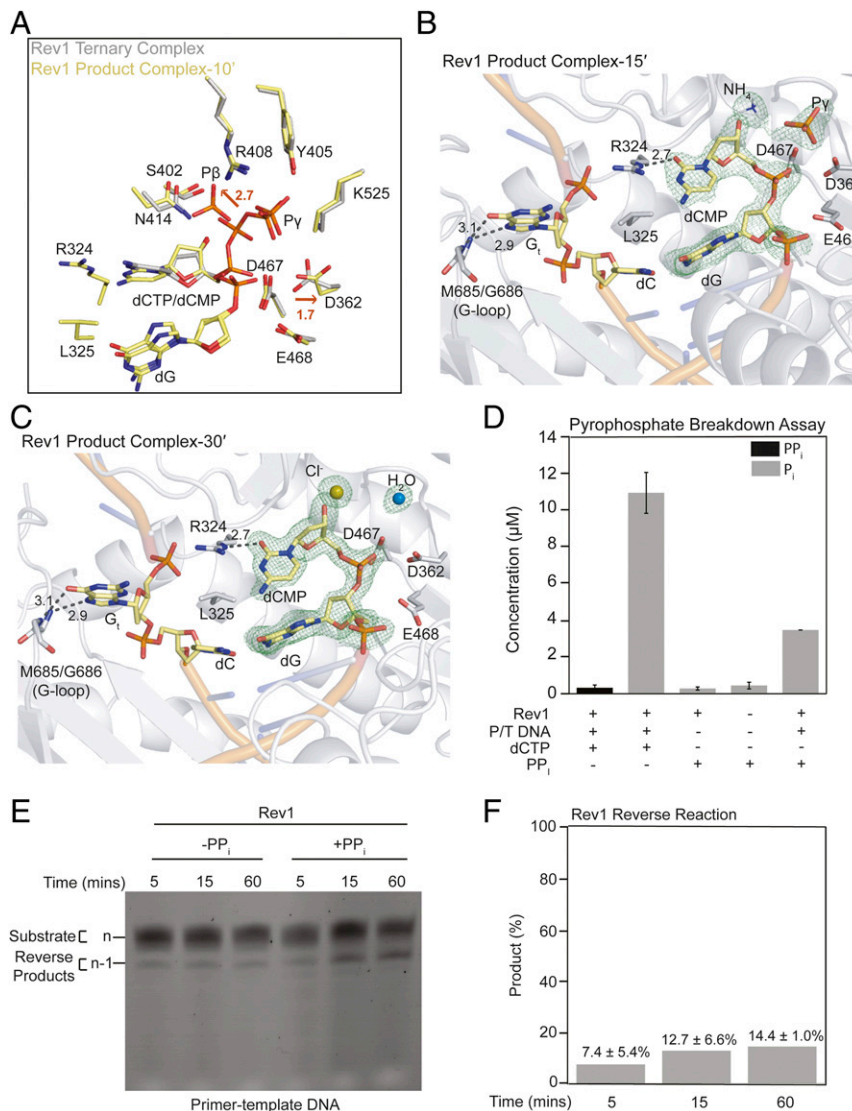
Fig. 4. PP$_i$ breakdown and disassociation in the Rev1 active site. (*A*) A focused view of the PP$_i$ movements in the active site of the product complex after a 10-min soak (yellow sticks) with an overlay of the Rev1 ternary complex (gray sticks) shown for reference. Red arrows and distances (Å) are indicated to highlight significant differences between the two structures. An active site close-up of the Rev1 product complex after a (*B*) 15-min and (*C*) 30-min soak in MgCl$_2$. The nucleic acid residues are shown in yellow and Rev1 in gray. An *Fo–Fc* OMIT map contoured at σ = 3.0 is shown as a green mesh. Key residues are indicated. (*D*) The concentrations of pyrophosphate (PP$_i$) and monophosphate (P$_i$) generated in solution during the Rev1 primer extension assay initiated with dCTP or PP$_i$. The "+" denotes components present in each reaction and the "−" denotes the components absent from each reaction. These values represent the average and standard deviation of at least three replicate experiments. (*E*) A representative reverse reaction assay for Rev1. (*F*) Quantification of the reverse reaction assay for Rev1. Values represent the mean and standad deviation from three replicate experiments.

polymerase. Our structure of the Rev1 product complex shows that Rev1 does not do this. The G$_t$ remains extrahelical in the Rev1 product complex, and the incorporated dCMP residue has shifted by ∼2 Å. This results in the loss of planarity between the incorporated dCMP and the side chain of R324 and the weakening of the hydrogen bonds between the dCMP and R324. This suggests that Rev1 must dissociate from the DNA before the incorporated dCMP can base pair with the template G. Furthermore, this dissociation may be facilitated by the movement of the primer terminus after catalysis that weakens the hydrogen bonds between R324 and the incorporated dCMP.

The Role of PP$_i$ Hydrolysis in Polymerase Function. The canonical nucleotidyl transfer reaction results in phosphodiester bond formation and the generation of PP$_i$. The PP$_i$ is subsequently released from the polymerase active site and hydrolyzed to monophosphates

by pyrophosphatases (36, 37). However, evidence for PP$_i$ hydrolysis in the active site of a DNA polymerase was recently described for DNA Pol IV, indicating some DNA polymerases have this intrinsic activity (32). Our data indicate that Rev1 also hydrolyzes PP$_i$ in the active site after phosphodiester bond formation has occurred. PP$_i$ hydrolysis in the active site of a DNA polymerase is proposed to make the DNA synthesis reaction energetically favorable (32, 38). In the case of Rev1, it is likely important for driving the forward reaction in two ways. First, it makes phosphodiester bond formation more energetically favorable without the need for a pyrophosphatase enzyme, as was hypothesized for DNA Pol IV. Second, it prevents the reverse reaction of pyrophosphorolysis, which can remove an added nucleotide (27, 33–35, 39).

Interestingly, the third metal seen in the product state of other polymerases studied by time-lapse crystallography, which has been proposed to play a role in facilitating catalysis by stabilizing
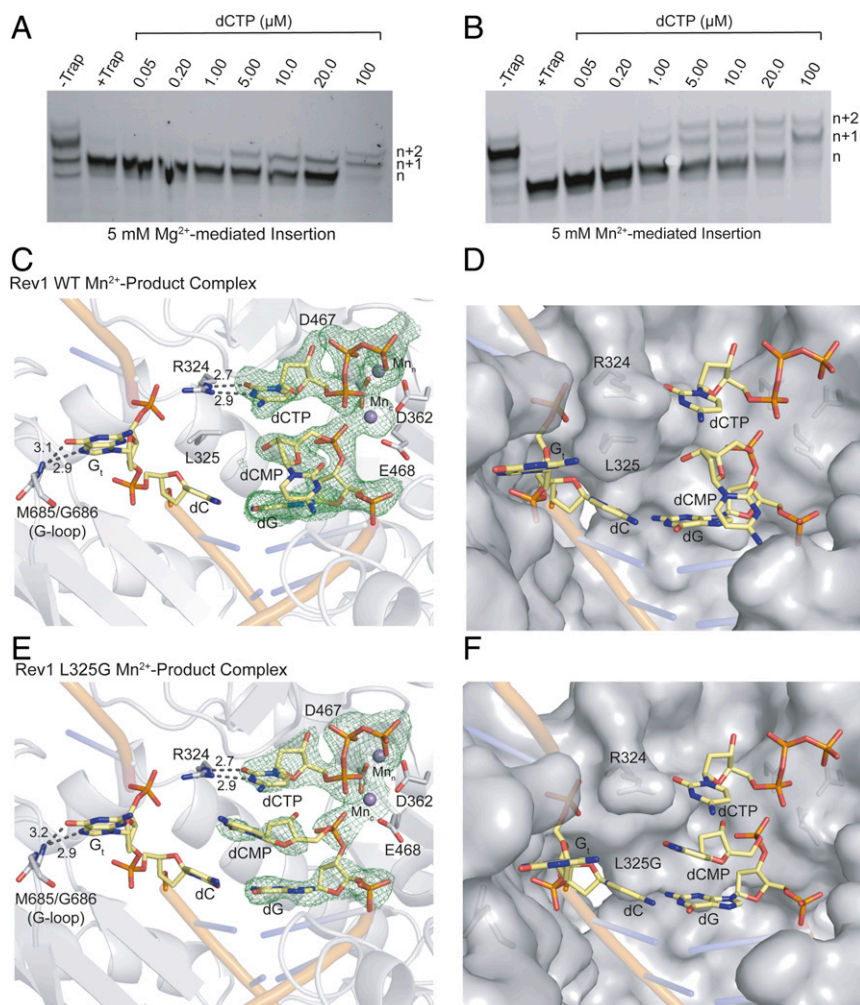
Fig. 5. Rev1 processivity. The Rev1 processivity assay in the presence of MgCl$_2$ (*A*) or MnCl$_2$ (*B*). Each processivity assay was repeated at least three times. (*C*) An active site close-up of the Rev1 product complex after a 240-min soak in MnCl$_2$. The nucleic acid residues are shown in yellow, Mn^{2+} in purple, and Rev1 in gray. An *Fo–Fc* OMIT map contoured at σ = 3.0 is shown as a green mesh. The inserted dCMP, second bound dCTP, and key residues are indicated. (*D*) The same structure and view as in *C* with Rev1 shown in a gray surface representation. (*E*) An active site close-up of the L325G Rev1 product complex after a 20-min soak in MnCl$_2$. The nucleic acid residues are shown in yellow, Mn^{2+} in purple, and Rev1 in gray. An *Fo–Fc* OMIT map contoured at σ = 3.0 is shown as a green mesh. The inserted dCMP, second bound dCTP, and key residues are indicated. (*F*) The same structure and view as in *E* with Rev1 shown in a gray surface representation.

the product state and preventing the reverse reaction (26–31), was not seen during Rev1-mediated insertion of dCTP. The observed breakdown of PP$_i$ in the active site of Rev1 may explain why a third metal is not seen during Rev1-mediated insertion. This is consistent with DNA Pol IV, which also did not contain a third metal in the product state for Mg^{2+}-facilitated insertion (32). However, it is possible that PP$_i$ hydrolysis leads to a short-lived state containing the third product metal that we were unable to capture in the structural snapshots presented here. Ultimately, hydrolyzing PP$_i$ after phosphodiester bond formation would likely commit a DNA polymerase to the forward DNA synthesis reaction.

Biological Implications for TLS. TLS polymerases have substantially lower fidelity than any other family of DNA polymerases. However, the low fidelity is balanced by the ability to bypass several types of DNA lesions that prove difficult for replicative polymerases to handle. Rev1 is an extreme example of a low-fidelity polymerase, as it preferentially inserts cytosines regardless of the templating base. Until now, the mechanism that prevents extensive mutagenic dCMP insertions once Rev1 is recruited to stalled

replication forks was unclear. Our crystal structures of the Rev1/DNA product state reveal the G$_t$ remains extrahelical even after catalysis, indicating that translocation to the next base is unable to occur. Consistently, Rev1 largely inserts only a single nucleotide in the presence of Mg^{2+} in solution before dissociating from the DNA. Although a second dCMP insertion in the presence of Mn^{2+} is observed in solution, our crystallographic data show Rev1 accomplishes this through reorganization of the primer DNA strand for binding a second dCTP without reincorporation of the G$_t$ into the DNA helix. This indicates the extrahelical templating base impairs Rev1 processivity, which ultimately prevents additional aberrant cytosine insertions after initial lesion bypass.

The TLS pathway requires the recruitment of specialized DNA polymerases that will bypass and extend from the DNA lesion prior to restarting the stalled replication fork (14). This necessitates the assembly and organization of the TLS machinery at a stalled replication fork. Rev1 is a critical player in organizing the TLS machinery as it interacts with monoubiquitinated PCNA and multiple other TLS polymerases, such as Pol η, Pol κ, and Pol ζ (11, 12). It is interesting to speculate

whether the nonprocessive nature of Rev1 facilitates the polymerase switch during TLS. For example, this may provide time for Rev1 to recruit another TLS polymerase capable of bypassing different types of DNA lesions. This could also serve as an opportunity to recruit Pol ζ, which would efficiently extend from the bypassed DNA lesion (13). Importantly, inhibiting the interaction of Rev1 with other TLS polymerases was recently shown as a promising therapeutic target in cancer (40–42). Therefore, future work is necessary to fully understand the interplay between the nonprocessive nature of Rev1 and the scaffolding function during the polymerase switch.

Methods

Preparation of DNA. For X-ray crystallography, 5′-ATC-GCT-ACC-ACA-CCC-CT-3′ (template strand) and 5′-GGG-GTG-TGG-TAG-3′ (primer strand) oligonucleotides were annealed in 1× TE (10 mM Tris- pH 8.0 and 1 mM EDTA) by heating to 90 °C for 5 min before cooling to 4 °C using a linear gradient (−1 °C min⁻¹). To generate the fluorescein-labeled DNA substrate for steady state kinetics and the Rev1 processivity assay, the 5′-GTA-CCC-GGG-GAT-CCG-TAC-GCC-GCA-TCA-GCT-GCA-G-3′ (template strand) and 5′-FAM-CTG-CAG-CTG-ATG-CGG-3′ (primer strand) oligonucleotides were annealed in 1× TE by heating to 90 °C for 5 min, cooling to 65 °C for 5 min before cooling to 10 °C using a linear gradient (−1 °C min⁻¹). To generate the unlabeled trap DNA for processivity assays and the PP$_i$ breakdown assays, the 5′-GTA-CCC-GGG-GAT-CCG-TAC-GCC-GCA-TCA-GCT-GCA-G-3′ and 5′-CTG-CAG-CTG-ATG-CGG-3′ oligonucleotides were annealed in 1× TE by heating to 90 °C for 5 min, cooling to 65 °C for 5 min before cooling to 4 °C using linear gradient (−1 °C min⁻¹). To generate the DNA for Rev1 reverse reaction assays, the 5′-GTA-CCC-GGG-GAT-CCG-TAC-GCC-GCA-TCA-GCT-GCA-G-3′ and 5′-CTG-CAG-CTG-ATG-CGG-C-3′ oligonucleotides were annealed in 1× TE by heating to 90 °C for 5 min, cooling to 65 °C for 5 min before cooling to 4 °C using linear gradient (−1 °C min⁻¹). To generate the gapped DNA for polymerase β reverse reaction assays, the 5′-GTA-CCC-GGG-GAT-CCG-TAC-CCG-CAT-CAG-TCG-CAG-3′ and 5′-FAM-CTG-CAG-CTG-ATG-CG-3′ and 5′-pGTA-CGG-ATC-CCG-GGT-AC-3′ oligonucleotides were annealed in 1× TE by heating to 90 °C for 5 min, cooling to 65 °C for 5 min before cooling to 4 °C using linear gradient (−1 °C min⁻¹). All DNA substrates were purchased from Integrated DNA Technologies.

Cloning, Expression, and Purification of Rev1. The yeast Rev1 construct (residues 305–746) was purchased from GenScript. All Rev1 proteins were expressed in BL21(DE3) plysS *Escherichia coli* cells (Invitrogen). Cells were grown at 37 °C until an OD$_{600}$ ∼0.7 was reached and protein expression induced with 0.1 mM isofopropyl-β-ᴅ-thiogalactopyranoside (IPTG) at 20 °C overnight. Cell pellets were frozen and stored at −20 °C. For lysis, Rev1 cell pellets were resuspended in a lysis buffer containing 50 mM Hepes (pH 7.4), 150 mM NaCl, 1 mM EDTA, 1 mM DTT, and a mixture of protease inhibitors (AEBSF, leupeptin, benzamidine, pepstatin A). The cells were lysed via sonication, lysate was cleared at 24,000 × g for 1 h and the supernatant incubated with glutathione agarose resin (Goldbio) for 2 h. The protein was washed on the glutathione beads with a high salt buffer containing 50 mM Hepes and 1 M NaCl and protein cleaved overnight using PreScission Protease. The cleaved Rev1 protein was purified by cation-exchange chromatography using a POROS HS column (GE Health Sciences) and eluted from the column using a linear gradient of a buffer containing 1 M NaCl and 50 mM Hepes (pH 7.4). Rev1 was further purified by gel filtration using a HiPrep 16/60 Sephacryl S-200 HR (GE Health Sciences) in a buffer containing 250 mM NaCl and 50 mM Tris (pH 8.0). The purified Rev1 protein was frozen and stored at −80 °C. All protein concentrations were determined by absorbance at 280 nM using a NanoDrop One UV–Vis Spectrophotometer (Thermo Scientific).

X-Ray Crystallography. For X-ray crystallography, 5′-ATC-GCT-ACC-ACA-CCC-CT-3′ (template strand) and 5′-GGG-GTG-TGG-TAG-3′ (primer strand) oligonucleotides were used. The annealed DNA substrate (1.15 mM) was mixed with Rev1 protein (5 to 6 mg mL⁻¹) and the Rev1-DNA binary crystals obtained in a condition with the reservoir containing 15 to 23% PEG3350 and 200 mM ammonium nitrate using the sitting-drop vapor diffusion method. The Rev1-DNA binary crystals were transferred to a cryoprotectant containing reservoir solution and 25% glycerol. Data were collected at 100 K on a Rigaku MicroMax-007 HF rotating anode diffractometer equipped with a Dectris Pilatus3R 200K-A detector system at a wavelength of 1.54 Å.

Initial models were generated by molecular replacement using a previously solved Rev1/DNA ternary complex (PDB ID code 5WM1) as a reference structure. Subsequent refinement was carried out using PHENIX and model building with Coot. All structure figures were generated using PyMOL (Schrödinger).

Steady-State Kinetics. The primer extension reactions for steady state kinetic analysis were performed using a fluorescein-labeled oligonucleotide 5′-GTA-CCC-GGG-GAT-CCG-TAC-GCC-GCA-TCA-GCT-GCA-G-3′ (template strand) and 5′-FAM-CTG-CAG-CTG-ATG-CGG-3′ (primer strand). The reactions were performed using 10 nM Rev1 protein and 100 nM DNA substrate in a buffer containing 25 mM Tris (pH 8.0), 100 mM KCl, 5 mM MgCl₂, 1 mM DTT, and 100 μg mL⁻¹ BSA. Initiation of the reactions were done by addition of dCTP at varying concentrations (WT: 1, 2, 3, 4, 5, and 10 μM and R518A: 1, 5, 7.5, 10, 15, 25, 100, and 200 μM) for 15 min and quenched using a loading dye containing 80% formamide 100 mM EDTA, 0.25 mg ml⁻¹ bromophenol blue and 0.25 mg mL⁻¹ xylene cyanol. Samples were heated to 95 °C and subsequently run on a 22% denaturing polyacrylamide gel. The gel was imaged using a Typhoon FLA 9500 imager (GE Health Sciences) and data processed in ImageJ. The steady state kinetics curves were fit using the Michalis–Menten equation: $v = V_{max}[dCTP]/K_m[dCTP]$.

PP$_i$ Breakdown Assay. The primer extension reactions for PP$_i$ breakdown used oligonucleotides 5′-GTA-CCC-GGG-GAT-CCG-TAC-GCC-GCA-TCA-GCT-GCA-G-3′ and 5′-CTG-CAG-CTG-ATG-CGG-3′. Rev1 primer extension reactions were performed using 250 nM Rev1 and 15 μM DNA substrate in a buffer containing 25 mM Tris (pH-8.0), 5 mM DTT, 100 μM EDTA, and 10% glycerol. The reactions were initiated by addition of 5 mM MgCl₂ and 1 mM dCTP for one hour before quenching with 20 mM EDTA. For PP$_i$ detection, the quenched reactions were incubated with a fluorogenic PP$_i$ sensor (MAK168, Sigma Aldrich) for 30 min. The fluorescence intensity was measured (λex = 316 nm and λem = 456 nm) using a Horiba FluoroMax-4 Fluorimeter and the concentration of PP$_i$ in the samples were determined from a standard curve generated from using purified PP$_i$. For monophosphate detection, the reactions were incubated with Malachite green dye (MAK308, Sigma Aldrich) for 30 min. The absorbance of the samples was collected at 620 nM using a NanoDrop One UV–Vis Spectrophotometer (Thermo Scientific) and the concentration of monophosphate determined using a standard curve generated from purified monophosphate.

Rev1 Processivity Assay. The primer extension reactions for Rev1 processivity analysis were performed using a fluorescein-labeled oligonucleotide 5′-GTA-CCC-GGG-GAT-CCG-TAC-GCC-GCA-TCA-GCT-GCA-G-3′ (template strand) and 5′-FAM-CTG-CAG-CTG-ATG-CGG-3′ (primer strand). The reactions were carried out using 100 nM Rev1, 100 nM DNA substrate and increasing concentrations of dCTP (0.05 to 100 μM) in a buffer containing 25 mM Tris (pH 8.0), 5 mM DTT, 100 μM EDTA, and 10% glycerol. The reactions were initiated using 5 mM Mg²⁺ or 5 mM Mn²⁺, 15 μM spermidine, and 15 μM trap DNA made from oligonucleotides 5′-GTA-CCC-GGG-GAT-CCG-TAC-GCC-GCA-TCA-GCT-GCA-G-3′ and 5′-CTG-CAG-CTG-ATG-CGG-3. The reactions were quenched using a loading dye containing 80% formamide 100 mM EDTA, 0.25 mg mL⁻¹ bromophenol blue, and 0.25 mg mL⁻¹ xylene cyanol. Samples were heated to 95 °C and subsequently run on a 22% denaturing polyacrylamide gel and the gel imaged using a Typhoon FLA 9500 imager (GE Health Sciences).

Reverse Reaction Assay. The Rev1 reverse reaction assay used oligonucleotides 5′-GTA-CCC-GGG-GAT-CCG-TAC-GCC-GCA-TCA-GCT-GCA-G-3′ and 5′-CTG-CAG-CTG-ATG-CGG-C-3′. The DNA polymerase β reverse-reaction assay used oligonucleotides 5′-GTA-CCC-GGG-GAT-CCG-TAC-CCG-CAT-CAG-TCG-CAG-3′ and 5′-FAM-CTG-CAG-CTG-ATG-CG-3′ and 5′-pGTA-CGG-ATC-CCG-GGT-AC-3′. Human WT DNA polymerase β was overexpressed from a pET-30 vector in the BL21-CodonPlus(DE3)-RP *E. coli* strain. The purification of polymerase β was carried out as previously described (43).

The reverse reactions were carried out using 500 nM protein, 50 nM DNA substrate, and 10 mM MgCl₂ in a buffer containing 25 mM Tris (pH 8.0) and 125 mM NaCl. The reactions were initiated with 1 mM PP$_i$ and quenched using a loading dye containing 80% formamide 100 mM EDTA, 0.25 mg mL⁻¹ bromophenol blue and 0.25 mg mL⁻¹ xylene cyanol. Samples were heated to 95 °C and subsequently run on a 22% denaturing polyacrylamide gel and the gel imaged using a Typhoon FLA 9500 imager (GE Health Sciences).

MD Simulations. MD simulations were performed for Rev1 and DNA complexes in explicit water solvent. Model preparation and simulations were

performed using the AMBER v16 suite of programs for biomolecular simulations (44). AMBER's *ff14SB* (45) force-fields were used for all simulations. MD simulations were performed using NVIDIA graphical processing units and AMBER's *pmemd.cuda* simulation engine using protocols published previously (46, 47).

A total of three separate simulations were performed (for binary, ternary, and product complexes) based on the X-ray crystal structures determined in this study. The missing hydrogen atoms were added by AMBER's *tleap* program. After processing the coordinates of the protein and substrate, all systems were neutralized by addition of counter ions and the resulting system were solvated in a rectangular box of SPC/E water, with a 10 Å minimum distance between the protein and the edge of the periodic box. The prepared systems were equilibrated using a protocol described previously (48). The equilibrated systems were then used to run 1.0 μs of production MD under constant energy conditions (NVE ensemble). The use of NVE ensemble is preferred as it offers better computational stability and performance (49). The production simulations were performed at a temperature of 300 K. As NVE ensemble was used for production runs, these values correspond to initial temperature at start of simulations. Temperature adjusting thermostat was not used in simulations; over the course of 1.0-μs simulations, the temperature fluctuated around 300 K with RMS fluctuations between 2 and 4 K, which is typical for well-equilibrated systems. A total of 1,000 conformational snapshots (stored every 1,000 ps) collected for each system was used for analysis.

RMSF10 calculations. Root mean square fluctuations (RMSF) were computed based on the conformational snapshots collected during the MD simulations. To identify global motions on slower time-scales from MD, for each of the three systems the fluctuations associated with the first (slowest) 10 quasiharmonic modes ($RMSF_{10}$) were also computed and aggregated. It is well known that slowest 10 modes contribute to the majority of fluctuations in proteins (>80%) and the use of $RMSF_{10}$, instead of all modes (RMSF), removes the faster stochastic motions of the protein, allowing focus on intrinsic dynamics of proteins (50). Both of these calculations were performed using AMBER's *ptraj* analysis program. All trajectory conformations were first aligned to a common structure, to remove any translation and overall molecular rotation during the simulations.

Protein–substrate interactions. The energy for the Rev1–DNA interactions ($E_{Rev1-DNA}$) were calculated as a sum of electrostatic (E_{el}) and van der Waals energy (E_{vdw}) between atom pairs, based on an approach developed in previous publications (51, 52). All Rev1 and DNA atom pairs were included in the calculations and resulting interaction energies were summed up per residue pair. The energies were calculated for 1,000 snapshots, every 1,000 ps, sampled during the full 1.0-μs simulation and were averaged over these 1,000 snapshots.

Data Availability. The X-ray crystal structures have been deposited in the Protein Data Bank, www.wwpdb.org (PDB ID codes 6X6Z and 6X70–6X77).

1. S. Wu, W. A. Beard, L. G. Pedersen, S. H. Wilson, Structural comparison of DNA polymerase architecture suggests a nucleotide gateway to the polymerase active site. *Chem. Rev.* **114**, 2759–2774 (2014).
2. E. Delagoutte, DNA polymerases: Mechanistic insight from biochemical and biophysical studies. *Front. Biosci.* **17**, 509–544 (2012).
3. N. M. Hoitsma et al., Structure and function relationships in mammalian DNA polymerases. *Cell. Mol. Life Sci.* **77**, 35–59 (2020).
4. E. T. Kool, Active site tightness and substrate fit in DNA replication. *Annu. Rev. Biochem.* **71**, 191–219 (2002).
5. M. W. Schmitt, Y. Matsumoto, L. A. Loeb, High fidelity and lesion bypass capability of human DNA polymerase delta. *Biochimie* **91**, 1163–1172 (2009).
6. J. F. Lemontt, Mutants of yeast defective in mutation induced by ultraviolet light. *Genetics* **68**, 21–33 (1971).
7. H. Ohmori et al., The Y-family of DNA polymerases. *Mol. Cell* **8**, 7–8 (2001).
8. W. A. Beard, S. H. Wilson, Structure and mechanism of DNA polymerase β. *Biochemistry* **53**, 2768–2780 (2014).
9. W. A. Beard, S. H. Wilson, "DNA polymerase β, eukaryotic" in *Encyclopedia of Biological Chemistry*, W. Lennarz, M. D. Lane, Eds. (Elsevier Science, San Diego, CA, 2013), Vol. 2, pp. 82–86.
10. T. Schlick, K. Arora, W. A. Beard, S. H. Wilson, Perspective: Pre-chemistry conformational changes in DNA polymerase mechanisms. *Theor. Chem. Acc.* **131**, 1287 (2012).
11. C. Guo et al., REV1 protein interacts with PCNA: Significance of the REV1 BRCT domain in vitro and in vivo. *Mol. Cell* **23**, 265–271 (2006).
12. E. Ohashi et al., Interaction of hREV1 with three human Y-family DNA polymerases. *Genes Cells* **9**, 523–531 (2004).
13. R. E. Johnson, M. T. Washington, L. Haracska, S. Prakash, L. Prakash, Eukaryotic polymerases ι and ζ act sequentially to bypass DNA lesions. *Nature* **406**, 1015–1019 (2000).
14. K. T. Powers, M. T. Washington, Eukaryotic translesion synthesis: Choosing the right tool for the job. *DNA Repair (Amst.)* **71**, 127–134 (2018).
15. D. T. Nair, R. E. Johnson, L. Prakash, S. Prakash, A. K. Aggarwal, Protein-template-directed synthesis across an acrolein-derived DNA adduct by yeast Rev1 DNA polymerase. *Structure* **16**, 239–245 (2008).
16. M. T. Washington et al., Efficient and error-free replication past a minor-groove N2-guanine adduct by the sequential action of yeast Rev1 and DNA polymerase zeta. *Mol. Cell. Biol.* **24**, 6900–6906 (2004).
17. M. E. Wiltrout, G. C. Walker, The DNA polymerase activity of Saccharomyces cerevisiae Rev1 is biologically significant. *Genetics* **187**, 21–35 (2011).
18. Y. Zhang et al., Response of human REV1 to different DNA damage: Preferential dCMP insertion opposite the lesion. *Nucleic Acids Res.* **30**, 1630–1638 (2002).
19. J.-Y. Choi, F. P. Guengerich, Kinetic analysis of translesion synthesis opposite bulky N2- and O6-alkylguanine DNA adducts by human DNA polymerase REV1. *J. Biol. Chem.* **283**, 23645–23655 (2008).
20. J. R. Nelson, C. W. Lawrence, D. C. Hinkle, Deoxycytidyl transferase activity of yeast REV1 protein. *Nature* **382**, 729–731 (1996).
21. A. Vaisman, R. Woodgate, Translesion DNA polymerases in eukaryotes: What makes them tick? *Crit. Rev. Biochem. Mol. Biol.* **52**, 274–303 (2017).
22. D. T. Nair, R. E. Johnson, L. Prakash, S. Prakash, A. K. Aggarwal, Rev1 employs a novel mechanism of DNA synthesis using a protein template. *Science* **309**, 2219–2222 (2005).
23. M. K. Swan, R. E. Johnson, L. Prakash, S. Prakash, A. K. Aggarwal, Structure of the human Rev1-DNA-dNTP ternary complex. *J. Mol. Biol.* **390**, 699–709 (2009).
24. D. T. Nair, R. E. Johnson, L. Prakash, S. Prakash, A. K. Aggarwal, DNA synthesis across an abasic lesion by yeast REV1 DNA polymerase. *J. Mol. Biol.* **406**, 18–28 (2011).
25. O. Rechkoblit, A. Kolbanovskiy, H. Landes, N. E. Geacintov, A. K. Aggarwal, Mechanism of error-free replication across benzo[a]pyrene stereoisomers by Rev1 DNA polymerase. *Nat. Commun.* **8**, 965 (2017).
26. B. D. Freudenthal et al., Uncovering the polymerase-induced cytotoxicity of an oxidized nucleotide. *Nature* **517**, 635–639 (2015).
27. B. D. Freudenthal, W. A. Beard, D. D. Shock, S. H. Wilson, Observing a DNA polymerase choose right from wrong. *Cell* **154**, 157–168 (2013).
28. A. M. Whitaker, M. R. Smith, M. A. Schaich, B. D. Freudenthal, Capturing a mammalian DNA polymerase extending from an oxidized nucleotide. *Nucleic Acids Res.* **45**, 6934–6944 (2017).
29. J. A. Jamsen et al., Time-lapse crystallography snapshots of a double-strand break repair polymerase in action. *Nat. Commun.* **8**, 253 (2017).
30. T. Nakamura, Y. Zhao, Y. Yamagata, Y. J. Hua, W. Yang, Watching DNA polymerase η make a phosphodiester bond. *Nature* **487**, 196–201 (2012).
31. Y. Gao, W. Yang, Capture of a third Mg^{2+} is essential for catalyzing DNA synthesis. *Science* **352**, 1334–1337 (2016).
32. J. Kottur, D. T. Nair, Pyrophosphate hydrolysis is an intrinsic and critical step of the DNA synthesis reaction. *Nucleic Acids Res.* **46**, 5875–5885 (2018).
33. D. D. Shock, B. D. Freudenthal, W. A. Beard, S. H. Wilson, Modulating the DNA polymerase β reaction equilibrium to dissect the reverse reaction. *Nat. Chem. Biol.* **13**, 1074–1080 (2017).
34. B. J. Vande Berg, W. A. Beard, S. H. Wilson, DNA structure and aspartate 276 influence nucleotide binding to human DNA polymerase β. Implication for the identity of the rate-limiting conformational change. *J. Biol. Chem.* **276**, 3408–3416 (2001).
35. T. W. Kirby et al., Metal-induced DNA translocation leads to DNA polymerase conformational activation. *Nucleic Acids Res.* **40**, 2974–2983 (2012).
36. F. Lapenta et al., Escherichia coli DnaE polymerase couples pyrophosphatase activity to DNA replication. *PLoS One* **11**, e0152915 (2016).
37. A. Kornberg, T. Baker, *DNA Replication*, (WH Freeman and Company, 1992).
38. L. Peller, On the free-energy changes in the synthesis and degradation of nucleic acids. *Biochemistry* **15**, 141–146 (1976).
39. C. R. Burke, A. Lupták, DNA synthesis from diphosphate substrates by DNA polymerases. *Proc. Natl. Acad. Sci. U.S.A.* **115**, 980–985 (2018).
40. S. Nayak et al., Inhibition of the translesion synthesis polymerase REV1 exploits replication gaps as a cancer vulnerability. *Sci. Adv.* **6**, eaaz7808 (2020).

41. J. L. Wojtaszek et al., A small molecule targeting mutagenic translesion synthesis improves chemotherapy. Cell **178**, 152–159.e11 (2019).

42. N. Chatterjee et al., A stapled POL κ peptide targets REV1 to inhibit mutagenic translesion synthesis. Environ. Mol. Mutagen., 10.1002/em.22395 (2020).

43. W. A. Beard, S. H. Wilson, Purification and domain-mapping of mammalian DNA polymerase β. Methods Enzymol. **262**, 98–107 (1995).

44. D. A. Case et al., AMBER 15, (University of California, San Francisco, 2015).

45. J. A. Maier et al., ff14SB: Improving the accuracy of protein side chain and backbone parameters from ff99SB. J. Chem. Theory Comput. **11**, 3696–3713 (2015).

46. A. Ramanathan, P. K. Agarwal, M. Kurnikova, C. J. Langmead, An online approach for mining collective behaviors from molecular dynamics simulations. J. Comput. Biol. **17**, 309–324 (2010).

47. A. Ramanathan, A. J. Savol, P. K. Agarwal, C. S. Chennubhotla, Event detection and sub-state discovery from biomolecular simulations using higher-order statistics: Application to enzyme adenylate kinase. Proteins **80**, 2536–2551 (2012).

48. A. Ramanathan, P. K. Agarwal, Evolutionarily conserved linkage between enzyme fold, flexibility, and catalysis. PLoS Biol. **9**, e1001193 (2011).

49. D. A. Beck, V. Daggett, Methods for molecular dynamics simulations of protein folding/unfolding in solution. Methods **34**, 112–120 (2004).

50. A. Ramanathan, P. K. Agarwal, Computational identification of slow conformational fluctuations in proteins. J. Phys. Chem. B **113**, 16669–16680 (2009).

51. P. K. Agarwal, Cis/trans isomerization in HIV-1 capsid protein catalyzed by cyclophilin A: Insights from computational and theoretical studies. Proteins **56**, 449–463 (2004).

52. D. Gagné et al., Ligand binding enhances millisecond conformational exchange in xylanase B2 from Streptomyces lividans. Biochemistry **55**, 4184–4196 (2016).